Journal of Energy Storage 136 (2025) 118430

Contents lists available at ScienceDirect

Journal of Energy Storage

journal homepage: www.elsevier.com/locate/est

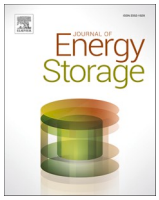

Research papers

Characterization of electrochemical processes in Na-based liquid metal batteries on different timescales

Renate Fetzer *, Alfons Weisenburger, Georg Müller

Institute for Pulsed Power and Microwave Technology (IHM), Karlsruhe Institute of Technology (KIT), Hermann-von-Helmholtz-Platz 1, 76344, Eggenstein-Leopoldshafen, Germany

ARTICLE INFO

Keywords:
Liquid metal battery (LMB)
Liquid sodium
Electrochemical impedance spectroscopy (EIS)
Overpotential
Diffusion
Charge-transfer resistance
Convection

ABSTRACT

The performance of liquid metal batteries (LMBs) is typically characterized by charge-discharging cycling. To gain fundamental understanding of the underlying electrochemical processes, this paper investigates in detail the buildup of the different overpotentials in an operating LMB. As model system, Na/LiCl-NaCl-KCl/Sb-Bi cells are assembled and tested. Cells with metal foam hosting the liquid Na are compared with foamless cells utilizing an insulating sheath. Based on data obtained by intermittent charging/discharging tests and electrochemical impedance spectroscopy, charge-transfer processes as well as diffusive and convective mass transport of Na inside the positive electrode are identified and quantified as function of the cell's state-of-charge. The convergence of the overpotential in the long-term/low-frequency limit is attributed to thermal convection if low currents are applied (impedance measurements). When applying larger currents such as the ones used for intermittent charging/discharging, an additional contribution attributed to solutal convection is observed and quantified. Thus, all processes relevant for the electrochemical performance of the tested Na-based LMB cells are captured, completely spanning the range from the millisecond timescale up to 1000 s.

1. Introduction

In recent years, new interest in liquid metal batteries (LMBs) arose due to their potential for large-scale stationary energy storage [1–4]. LMB cells combine the advantages of low-cost, easy scalability and temperature management, low maintenance, and long service life. Compared with other electrical storage systems, LMB cells provide fast transport and reaction kinetics, which allows high current densities.

Most liquid metal batteries researched today use lithium (Li) as negative electrode metal, which is typically combined with antimony (Sb) or Sb-containing alloys as positive electrode [5–11]. Other possibilities are, for instance, Na-based LMBs [12,13] using sodium instead of Li due to its high abundance in the earth crust and, thus, economic and environmental advantages over Li. Both Li- and Na-based LMB cells promise excellent electrochemical performance, which is typically demonstrated by charge-discharge cycling tests. From these cycling tests, important parameters of the cell such as its charge and discharge capacity, the material utilization, Coulombic and energy efficiencies, self-discharge, and long-term stability are obtained. However, fundamental understanding of the electrochemical processes in LMB cells is researched mainly numerically, while detailed experimental studies are rarely found.

The energy efficiency, obtained from cycling tests as a lump-sum value, is determined by the individual processes in the cell that result in the buildup of various overpotentials upon charging/discharging. For liquid metal batteries, the most prominent and experimentally most easily accessible overpotential is the ohmic overpotential (IR drop), with its main contribution stemming from the finite ionic conductivity of the electrolyte. At high current density or for large timescales, the mass transport overpotential gains significance. Generally, mass transport overpotentials build up whenever an inhomogeneous concentration of active species develops due to their limited speed of transport (diffusion, convection, migration). This can occur in the electrolyte or in the positive electrode. Fluid flow in an LMB cell can considerably enhance the mass transport of active species, thus homogenizing the concentration fields and lowering the mass transport overpotential. Extensive flow, however, can also lead to instabilities and short-circuiting. Therefore, the fluid dynamics in LMBs is of great interest and has been extensively researched in recent years [14–26]. In the electrolyte, the rather low ionic conductivity typically leads to Joule heating strong enough to

* Corresponding author.
E-mail address: renate.fetzer@kit.edu (R. Fetzer).

https://doi.org/10.1016/j.est.2025.118430
Received 14 January 2025; Received in revised form 24 July 2025; Accepted 5 September 2025
Available online 11 September 2025

cause significant thermal convection, which homogenizes the concentration of active ions and prevents the buildup of a considerable mass transport overpotential [15,16]. Noticeable thermal convection due to Joule heating is not expected in the positive electrode due to its high electric conductivity. On the contrary, Joule heating of the electrolyte typically leads to a stable temperature stratification in the positive electrode, which makes mass transport in the positive electrode most challenging. External heating from below might induce thermal convection also in the positive electrode [17]. Other measures to deliberately generate convection in the positive electrode are a specific design that promotes electro-vortex flow [18] or the application of an external magnetic field to enhance electromagnetically driven convection [19,20]. Finally, the inhomogeneous concentration itself might lead to convection, because the density of the positive electrode alloy depends on its composition, in particular on the concentration of the less dense negative electrode metal. Compositional or solutal convection results in an asymmetry between charging and discharging, as charging leads to an unstable density stratification while discharging results in a stable one [21,22]. Finally, the complex interplay between the described effects on the overall flow in the cell is of great relevance [22–26]. Despite the numerous numerical studies on the influence of flow on the operation of liquid metal batteries, experimental data are rarely analyzed in this respect. If at all, they are used to validate simulation models [16,20–22].

When fluid flow in the positive electrode is negligible and diffusion is the only relevant mass transport mechanism, the diffusion coefficient of the negative electrode metal might be obtained by intermittent charging/discharging tests (also called galvanostatic intermittent titration technique (GITT) or coulombic titration) from the slope in a plot of voltage versus the square-root of time or, less accurate, from the voltage difference at the beginning and at the end of the current steps. Only few studies are available in literature that give experimental results for the diffusion coefficient in an LMB [12,27,28]. However, detailed analysis of the mass transport overpotential in an LMB is rarely done, in particular no data are published regarding the involved timescales or the applicability of the formula used for analysis.

Processes that occur on short timescales (10 s and below) can be investigated by electrochemical impedance spectroscopy (EIS), a very powerful technique to gain fundamental understanding of fast processes in a cell. EIS is a well-established technique for studying cells with solid electrodes such as Li ion batteries (Lib) or lithium/sulfur (Li/S) battery cells. Here, one of the main interests lies in the activation overpotential, i.e., the charge-transfer reaction kinetics at the electrolyte-electrode interfaces. The corresponding feature in the Nyquist plot of impedance data is a well-pronounced semi-circle. For most battery types with solid electrodes, the biggest challenge of impedance data analysis is a proper assignment of the individual features to anode and cathode. Because of the similar timescales of anode and cathode activation overpotentials, both contributions often superpose to a single semi-circle. Possible solutions are a symmetric cell approach [29–33], the variation of single electrode properties, or an imposed temperature gradient along a full cell [34].

In contrast to cells with solid electrodes, EIS data of LMB cells are typically only rudimentarily analyzed, if measured at all. Because activation overpotentials of a liquid system have a much lower charge-transfer resistance compared with solid electrode systems, the corresponding semi-circle is often poorly pronounced and/or obscured by other processes or the scatter in the impedance data [7–11,27,28,35].

The present study uses Na//$SbBi_9$ LMB cells as model system to investigate the temporal evolution and magnitude of the mentioned overpotentials experimentally. Specific to these LMB cells is the liquid state of both electrodes in all states of charge (SOCs) tested. The Na-based LMBs are assembled in two different designs, a conventional design with a metal foam to host the negative electrode (liquid Na) and a foamless design where the negative electrode floats freely on top of the electrolyte. In addition to the standard electrochemical characterization of the cells by charge-discharge cycling tests, the galvanostatic intermittent titration technique and electrochemical impedance spectroscopy are performed, two electrochemical techniques that complement each other regarding the probed timescale. This allows identification and characterization of different processes in the cells, including diffusive and convective mass transport and charge-transfer reactions. The corresponding overpotentials are quantified as function of the cells' SOC for both charging and discharging.

2. Materials and methods

2.1. Materials

The electrochemically active materials of the LMB cells are Na, $SbBi_9$ alloy, and the salt mixture LiCl-NaCl-KCl (61-3-36 mol%). Antimony and bismuth, both with purity 99.99 %, were delivered by HMW Hauner GmbH & Co. KG in granular form. The $SbBi_9$ alloy was obtained by mixing the granules in the required ratio and amount in an alumina crucible. Then, the alloy was melted under oxygen-poor conditions in the COSTA facility [36] to remove any oxygen impurity from the alloy. After cooling down to room temperature in controlled atmosphere, the alloy was transported to a glovebox with controlled Ar atmosphere ($O_2 < 1$ ppm, $H_2O < 0.5$ ppm) for assembly of the LMB cells.

Sodium (purity 99.8 %) was obtained from Haines & Maassen Metallhandelsgesellschaft GmbH and further purified in the glovebox in a specially designed Na sink.

The salt LiCl (anhydrous, purity 99.9 %) was obtained from Apollo Scientific, NaCl (anhydrous, free-flowing, purity ≥99.0 %) from Honeywell, and KCl (purity ≥99.5 %) from Sigma-Aldrich. The salts were mixed in the specified ratio LiCl-NaCl-KCl (61-3-36 mol%) and dried inside the glovebox at 150 °C and 300 °C for at least 30 min each before melting.

2.2. Cell design and assembly

LMB cells with two different designs were investigated, as shown in Fig. 1. The design with foam, Fig. 1(a) and (b), utilized a Ni foam (diameter 40 mm, thickness 5 mm, porosity 50 PPI) to host the liquid sodium. After removal of surface oxides, the foam was immersed in liquid Na and the Na was forced into the pores of the foam by vacuum conditions. Then the foam was fixed to a foam holder with Mo wires. After pouring liquid $SbBi_9$ alloy and molten salt (see Table 1 for respective amounts) in the cell body made of stainless steel 316Ti, the cell cover holding the negative electrode was closed and hermetically sealed. In the foamless design, Fig. 1(c), a ceramic sheath was introduced to insulate the freely floating negative electrode from the cell body, which serves as positive current collector. Further details on the cells and their assembly can be found in Ref. [13].

For cell operation, the cells were placed in heating sleeves and heated from below to working temperature. Due to heat losses to the top, a temperature gradient existed inside the cells. For a nominal temperature of 530 °C, the temperature inside a cell with foam was measured to be 461 °C at a height of 7 mm above the cell bottom (note that the thickness of the positive electrode was 5 mm, see Table 1), 458 °C at 18 mm height (both measurements were located in the electrolyte), and around 380 °C at a height of 45 mm (vapor phase). Cell tests were performed at the nominal temperatures 530 °C and 500 °C, which means that the electrolyte had temperatures around 460 °C and 430 °C, respectively.

In this study, electrochemical data are analyzed in detail for three different cells, two cells with foam (D7 and D8) and one foamless cell (FL2). The cell names correspond to the ones in the previous study [13]. Specific parameters of the cells are given in Table 1. It should be noted that D7 was assembled with least oxygen in the system. The metal foam was cleaned from surface oxides directly before its further use and the atmosphere in the glovebox showed lower oxygen and humidity content

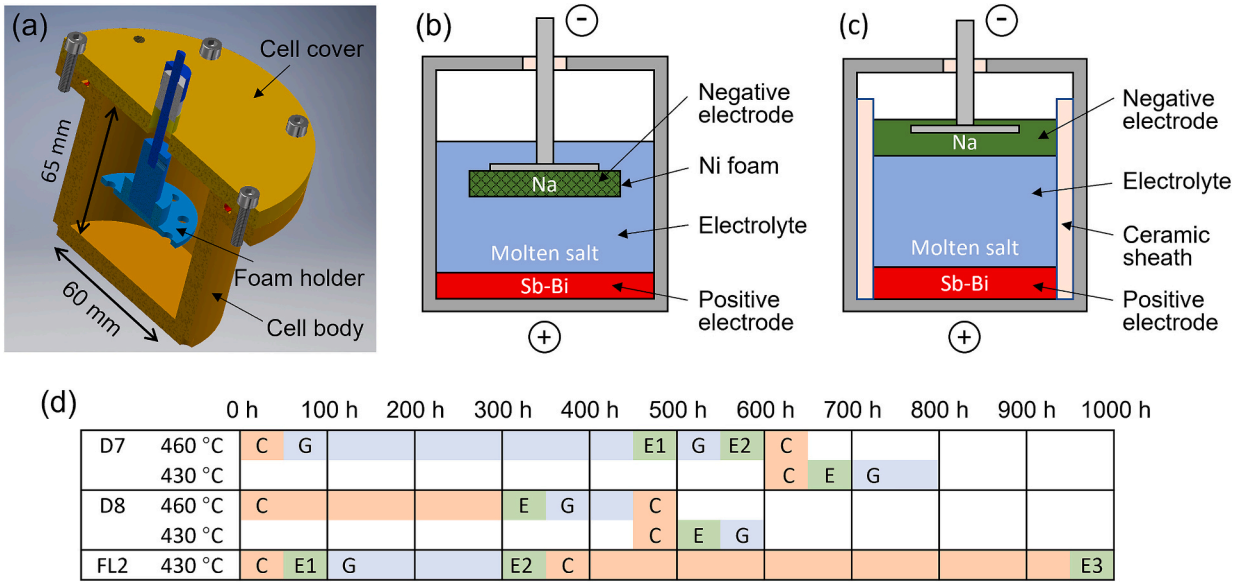

Fig. 1. Experimental details: (a) Drawing of solid cell components used for both designs, (b) sketch of LMB cell design with solid foam, (c) sketch of foamless design with insulating ceramic sheath, (d) timeline of cell tests (C – charge-discharge cycling tests, G – GITT measurements, E – EIS tests).

Table 1
Cell parameters with h_{SbBi9} the height of the positive electrode, d the distance between positive and negative electrode, S_{SbBi9} the positive electrode – electrolyte interfacial area, and S_{Na} the negative electrode – electrolyte interfacial area. In the design with foam, S_{Na} considers only the bottom side of the foam.

Cell name	m_{Na}	m_{SbBi9}	h_{SbBi9}	d	S_{SbBi9}	S_{Na}
D7	4.9 g	130 g	5 mm	14 mm	28.3 cm^2	12.6 cm^2
D8	4.2 g	130 g	5 mm	13 mm	28.3 cm^2	12.6 cm^2
FL2	30.4 g	108 g	6.5 mm	21 mm	18.1 cm^2	18.1 cm^2

than during assembly of the other cells. There might have been also some differences in the water content of the molten salts due to deviating drying durations.

2.3. Electrochemical tests

All cells were characterized by charge-discharge cycling, galvanostatic intermittent titration technique, and electrochemical impedance spectroscopy. Cycling and intermittent charging/discharging tests were performed with an Arbin electrochemical station (LBT21084HC), while a Gamry 5000E Potentiastat/Galvanostat was used for the EIS measurements. The timelines of the tests performed on the individual cells at the respective temperatures of the active liquids are shown in Fig. 1(d).

Charge-discharge cycling of the default cells D7 and D8 was performed with constant current – constant voltage (CCCV) charging and constant current (CC) discharging. Typical parameters of CCCV charging were a charging current between 1.8 and 2.8 A until an upper voltage limit of 1.1 V was reached, followed by CV charging at the upper voltage limit until the current dropped below 1.0 A. Discharging was done to a lower voltage limit of 0.5 V, which falls in the regime of deep discharge (all available Na was transferred to the positive electrode). The foamless cell FL2 was cycled with CC charging and CC discharging using a current of ±1.8 A and an upper voltage limit of 1.2 V. Various lower voltage limits were tested, with none of them reaching deep discharge (note the much higher amount of Na in the foamless cell).

For the GITT measurements, a series of constant current pulses was applied to the cell, each followed by a longer relaxation step where the cell was at rest. The voltage response of the cell was recorded throughout the entire tests. GITT was performed repeatedly for both charging and discharging. A current of ±0.5 A was used for the cells D7 and D8, while a higher current of ±0.7 A was used for cell FL2 due to its higher capacity. For all cells, the same duration of the current steps (1000 s) and the rest steps (2000 s) was chosen.

The EIS measurements were performed at different stages of charge (SOC). After reaching the desired SOC by charging or discharging, the cells were allowed to relax before starting the EIS measurement. Both the galvanostatic and the potentiostatic mode were used, i.e., either a small-amplitude alternating current or a small-amplitude alternating voltage was applied to the cell and the voltage respectively current response was recorded. After some initial tests, the excitation amplitudes were chosen small enough to stay within the linear response, i.e., the results were independent of the excitation amplitude and of the operation mode (galvanostatic or potentiostatic), and large enough to reduce the statistical noise and to obtain reliable data. Most EIS measurements were performed with an excitation current of 20 mA RMS amplitude in the frequency range 10 kHz to 0.01 Hz.

2.4. Theoretical background

When a battery is charged or discharged, the measured terminal voltage $U_t(t)$ deviates from the cell voltage U_0 at the current state-of-charge $SOC(t)$ due to the overpotentials $\eta_j(t)$ according to $U_t(t) = U_0(SOC(t)) + \sum_j \eta_j(t)$. Throughout this study, charge currents and overpotentials during charging are assigned positive values, while discharge currents and overpotentials are negative. Typical overpotentials $\eta_j(t)$relevant for a liquid metal battery are the ohmic overpotential $\eta_{ohm}(t) = I(t) \bullet R_0$ due to the ohmic cell resistance R_0, the activation overpotential $\eta_{act}(t)$, and the mass transport overpotential $\eta_{mt}(t)$.

The activation overpotential accounts for the processes at the electrode/electrolyte interfaces: current passes through the interface either as capacitive current charging/discharging the double layer capacitance C_{dl} or, in parallel, as Faraday current, which requires a charge transfer reaction. The finite speed of the charge transfer reaction is accounted for by the charge transfer resistance R_{ct}. Thus, an activation overpotential is typically modelled by an RC circuit in an equivalent circuit model, with the time constant $\tau = R_{ct}C_{dl}$ and the cutoff frequency $f_c = 1/(2\pi\tau)$.

In real cells, impedance data are often found to deviate from the behavior of an ideal RC circuit. In a Nyquist plot, data rather form a flattened semi-circle, which is more adequately modelled by a constant

phase element replacing the capacitance in an RC circuit. A constant phase element *CPE* has an impedance of the general form $Z_{CPE} = 1/(Y_0(i\omega)^{\alpha})$ with $0 < \alpha \leq 1$ (i is the imaginary unit and ω is the angular frequency). It reflects a generalization of capacitive behavior in electrochemical cells. The time constant of the corresponding "generalized RC circuit" (parallel circuit of R and *CPE*) is given by $\tau = (R \bullet Y_0)^{1/\alpha}$. The limit $\alpha = 1$ corresponds to an ideal capacitance, while $\alpha = 0.5$ corresponds to the infinite Warburg impedance. A Warburg element W with an impedance of $Z_W = \sqrt{2}A_W/\sqrt{i\omega}$ is typically used to model a mass transport overpotential caused by diffusion and corresponds to the behavior $dU_t \propto d\sqrt{t}$ observed after switching on a constant current.

Mass transport overpotentials $\eta_{mt}(t)$ are caused by the retarded transport of active species, e.g., of the ions in the electrolyte or of the negative electrode metal inside the positive electrode. In a liquid metal battery, the transport of active ions in the electrolyte is typically enhanced by considerable thermal convection due to Joule heating, which makes the electrolyte's contribution to the mass transport overpotential negligible [15,16]. Convection in the positive electrode, on the other hand, is usually less pronounced. If it is entirely negligible, diffusion of the negative electrode metal (here Na) inside the positive electrode (here Na-Sb-Bi alloy) is the only relevant transport mechanism. For an initially relaxed cell (i.e., constant Na concentration in the positive electrode) and a constant current I_0, the finite speed of Na diffusion results in a diffusive mass transport overpotential well approximated by [37]

$$\eta_{dmt}(t) = \frac{2I_0V_m}{SzF\sqrt{\pi D}}\left|\frac{dU_0}{dx}\right|\sqrt{t}. \quad (1)$$

Here, S is the surface area of the positive electrode (S_{SbBi9}), z is the number of charges per sodium ion ($z = 1$), F is the Faraday constant, D is the diffusion constant of Na in the Na-Sb-Bi alloy, $x = n_{Na}/(n_{Na} + n_{Sb} + n_{Bi})$ is the molar ratio of Na in the Na-Sb-Bi alloy, and $V_m = V/(n_{Na} + n_{Sb} + n_{Bi})$ is the molar volume of the Na-Sb-Bi alloy. Because of the finite thickness of the positive electrode, L, Eq. (1) is valid for $t \ll L^2/D$ only. For this timescale, the change of the average concentration in the electrode is negligible against the change at the electrode surface and the dependence of the cell voltage on the concentration can be linearized, i.e., $\frac{dU_0}{dc} = V_m\frac{dU_0}{dx}$ can be assumed constant.

3. Results

3.1. Charge-discharge cycling

The operation of all cells was started with charge-discharge cycling tests, cf. Fig. 1(d). As reported previously, the LMB cells need some time for stabilization, most probably due to impurities and side reactions [13]. After around 10 cycles or a few days of operation, stable cycling performance is obtained as shown in Fig. 2(a) and (b). For the cycling parameters used in the tests, a Coulombic efficiency >99 % and an energy efficiency around 60 % is obtained. Charge losses are caused by self-discharge of the cells due to a non-zero solubility of Na in the molten salt electrolyte. Typical values are around 10 mA for the investigated cells [13]. Responsible for the energy losses are the overpotentials.

The ohmic overpotential can be determined directly from the cycling tests. Fig. 2(c) shows the ohmic resistance R_0 of the cells obtained from exemplary IR drops at switching on the charging/discharging currents during cycling, plotted versus the total operation time as shown in Fig. 1 (d). FL2 shows a significantly higher value compared with D7 and D8 due to the larger distance between the electrodes and the smaller cross section, see Table 1. Additionally, the cells show some variations at early times, which are attributed to cell initialization as mentioned above. Cell D8 shows a much larger ohmic resistance initially, which declines to a stable plateau within 200 h. In addition, an asymmetry is observed between charging and discharging, which persists even after cell initialization. The strongest asymmetry is obtained for FL2 during cell initialization. The most stable values are found for cell D7.

3.2. Intermittent charging/discharging tests

Further characterization of the cells and the electrochemical processes during operation was done by intermittent charging/discharging, which allows to obtain well-defined cell states between the current pulses. All GITT tests were done after cell initialization, i.e., after the cells reached a stage of stable operation, see also timelines shown in Fig. 1(d). An example of a GITT measurement of cell D7 is shown in Fig. 3(a) and (b).

After each current pulse, the cell is allowed to relax until all overpotentials η_j are negligible. The measured voltage $U_t = U_0 + \sum_j \eta_j$ at the end of each relaxation step can thus be considered to equal the cell voltage U_0 at the respective state-of-charge. These data are plotted in Fig. 3(c) versus the molar concentration of Na in the positive electrode, $x = n_{Na}/(n_{Na} + n_{Sb} + n_{Bi})$. Self-discharge was taken into account when calculating x. It is noted that data of charging and discharging coincide as long as the Na content in the positive electrode remains below 20 mol %, which indicates a totally reversible and symmetric alloying/dealloying process in this concentration range. In addition, the cell voltage data are independent of temperature and of cell age within the investigated range. Note that a temperature dependence is excepted for significantly larger variations (100 K or more).

The data of the ohmic resistance R_0 determined from the IR drop at switching on the current of intermittent charging/discharging experiments are presented in Fig. 3(d). The values of R_0 are independent of the cell voltage U_0 (i.e., the cell's SOC) and of the direction of current. The only exception is obtained for cell D8 at 460 °C. Here, the ohmic resistance is considerably higher at charging than at discharging. The symmetry in all other cases is a significant difference to the data obtained from cycling tests (Fig. 2(c)).

Since the cell is in a relaxed state after each rest step and prior to each current pulse, GITT data further allow quantitative analysis of the

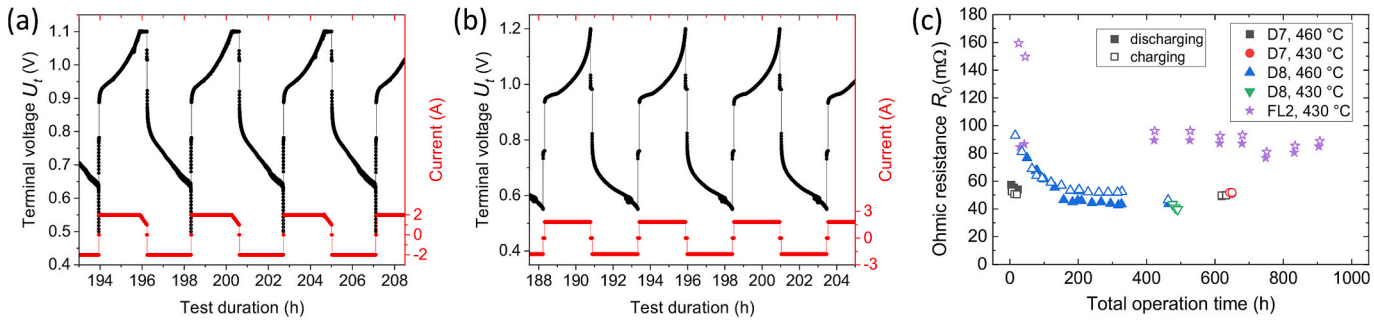

Fig. 2. Charge-discharge cycling tests: (a) Typical CCCV cycles of cell D8 at 460 °C, (b) typical CC cycles of cell FL2 at 430 °C, (c) ohmic resistance of all cells, obtained from IR drops of cycling tests.

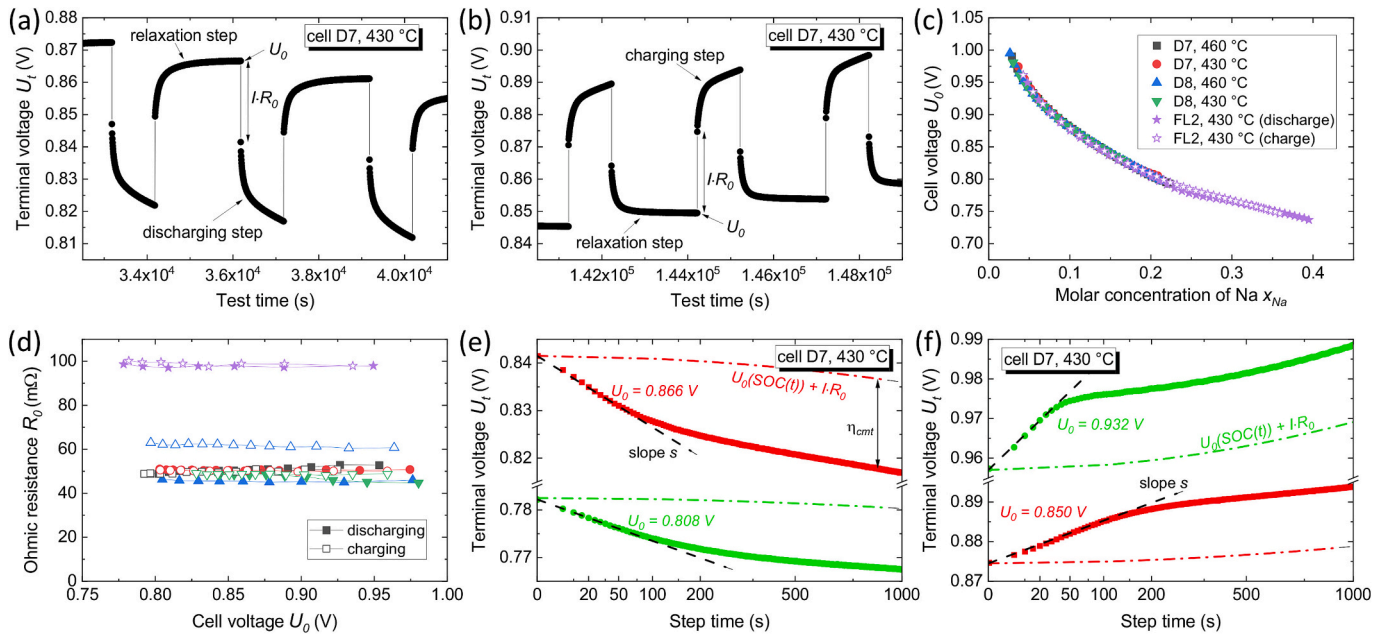

Fig. 3. Intermittent charging/discharging tests: (a), (b) Exemplary GITT data of D7 at 430 °C for discharging (a) and charging (b), (c) cell voltage as function of molar concentration of Na in the positive electrode alloy Na-Sb-Bi, (d) ohmic resistance obtained from IR drops of GITT data (the legend of (c) also applies to (d)), (e), (f) typical discharging (e) and charging (f) curves of GITT data plotted versus discharge/charge time (square-root scale). The red data in (e) and (f), respectively, correspond to the second current steps shown in (a) and (b), the green data are taken a few discharging/charging steps later. The black dashed lines mark straight-line fittings in the relevant time regime. The red and green dashed-dotted lines indicate the linearized evolution of $U_0(SOC(t)) + I \bullet R_0$. The parameter η_{cmt} in (e) indicates the roughly constant overpotential towards the end of the discharge step. (For interpretation of the references to colour in this figure legend, the reader is referred to the web version of this article.)

overpotentials η_i and their temporal evolution on the probed timescale of ~10 to 1000 s. The most commonly "diagnosed" and analyzed overpotential of GITT data is the diffusive mass transport overpotential $\eta_{dmt}(t)$, which is expected to build up proportionally to $\sqrt{t}$, see Eq. (1). As seen in the plot of the measured voltage U_t versus $\sqrt{t}$ in Fig. 3(e) and (f), the behavior $dU_t \propto d\sqrt{t}$ is indeed observed after the IR drop, indicating a regime of diffusive mass transport. However, the diffusive regime ends after less than 200 s and is replaced by a stage with roughly constant overpotential. Qualitatively similar behavior is observed for the other cells/temperatures.

The data in the diffusive regime with behavior $dU_t \propto d\sqrt{t}$ were fitted by a straight line in the plot of voltage versus $\sqrt{t}$, i.e., $U_t(t) = U_0 + \eta_{ohm} + s \bullet \sqrt{t}$. From the slope s the diffusion constant D was determined via Eq. (1). Respective results for all cells/temperatures are plotted in Fig. 4(a). The applicability limit of Eq. (1) due to the finite thickness of the positive electrode, L^2/D, is above 10,000 s for all cells and thus far beyond the timescale of the analyzed data. It is observed that the diffusion coefficient is different for each cell. However, there is no significant difference observed between charging and discharging. Neither does the diffusion coefficient systematically depend on the cell's SOC. The only cell that shows an apparent dependence on the cell voltage is cell D7 at 460 °C. In this case, however, the diffusive regime ends already prior to the second data point, see transition time between the diffusive regime and the regime with roughly constant overpotential, Fig. 4(b). This makes the analysis of the data D7, 460 °C in the diffusive regime unreliable, in particular for higher cell voltage.

As noted above, after the stage of diffusive mass transport with behavior $dU_t \propto d\sqrt{t}$, an almost constant total overpotential $\eta_{tot} = U_t(t) - U_0(SOC(t))$ is observed. This is attributed to the onset of convection in the positive electrode or, more precisely, to the onset of its relevance for mass transport, see also 4. Discussion. Convection increases the mass transport and reduces the related mass transport overpotential. Thus, from the total overpotential $\eta_{tot} = \eta_{ohm} + \eta_{cmt}$ at the end of the charging/discharging steps (cf. Fig. 3(e) and (f)), the convective mass transport overpotential η_{cmt} respectively the corresponding resistance $R_{cmt} = \eta_{cmt}/I$ was obtained, see Fig. 4(c). In contrast to the diffusive regime, the

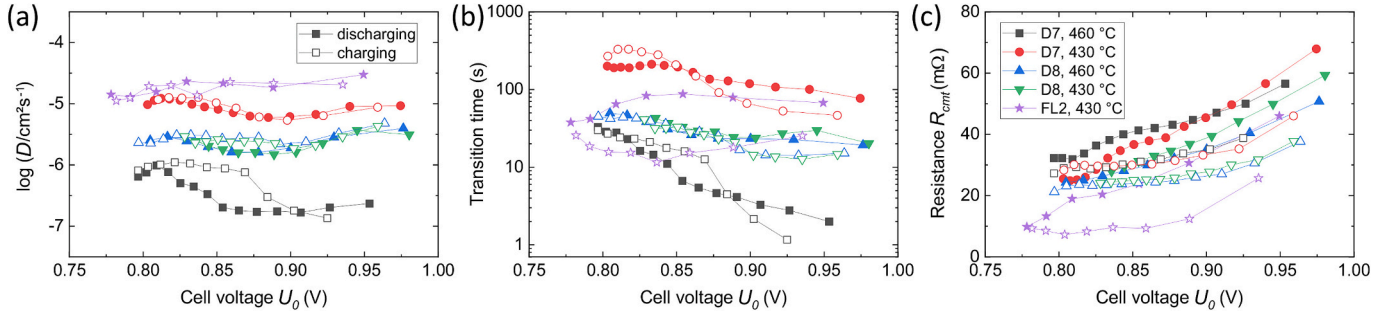

Fig. 4. Results of GITT data analysis: (a) Diffusion coefficient determined from the slope in the plot of U_t versus $\sqrt{t}$, see Fig. 3(e) and (f), (b) transition time between diffusive regime and regime with constant overpotential, (c) resistance R_{cmt} attributed to convective mass transport overpotential η_{cmt} obtained at the end of the charging/discharging steps. The given legends apply to all graphs.

convection-enhanced mass transport shows an asymmetry between charging and discharging: all cells show a reduced overpotential η_{cmt} for charging compared with discharging, indicating higher convection during charging. Additionally, η_{cmt} increases with increasing cell voltage. Interestingly, the smallest convective mass transport overpotential is obtained for charging the foamless cell FL2, indicating strongest convection among all cases considered. As further explored in the discussion, this could be related with a higher level of thermal convection in FL2 compared with D7/D8.

3.3. Electrochemical impedance spectroscopy

To complement the data obtained by intermittent charging/discharging, electrochemical impedance spectroscopy was performed on all cells. Compared with GITT, which characterizes the cell's overpotentials on the timescale of ~10 to 1000 s, EIS is more suitable to reveal processes at shorter times respectively higher frequencies. However, since only the linearized cell response is probed by EIS, differences between charging and discharging cannot be revealed.

Typical EIS data of different cells, each measured at different SOCs, are presented in Fig. 5. All cells show an impedance increase both at low frequencies (below ~1 Hz) and at very high frequencies (above ~1000 Hz), see $|Z|$ in the Bode plot (first row of Fig. 5). The increase at very high frequencies does not depend on the cell's SOC and is of inductive nature ($\Phi > 0$, see Bode plot in Fig. 5, second row). It is attributed to cables and is not further analyzed. The increase at low frequencies strongly depends on the cell's SOC and has capacitive nature ($\Phi < 0$). Some cells reveal an additional impedance change at medium frequencies, which also depends on the SOC and is of capacitive nature. The cutoff frequency of this additional impedance drop strongly deviates from cell to cell and is in the range ~1–1000 Hz.

Fig. 5, third row, shows the impedance data in a Nyquist plot. The inductive behavior ($Z_i > 0$) at very high frequencies is cut off and the data showing capacitive behavior ($Z_i < 0$) are presented on a 1:1 scale of x- and y-axis. The data of both cells with foam, D7 and D8, show a superposition of an ohmic resistance (x-intercept) and two more or less

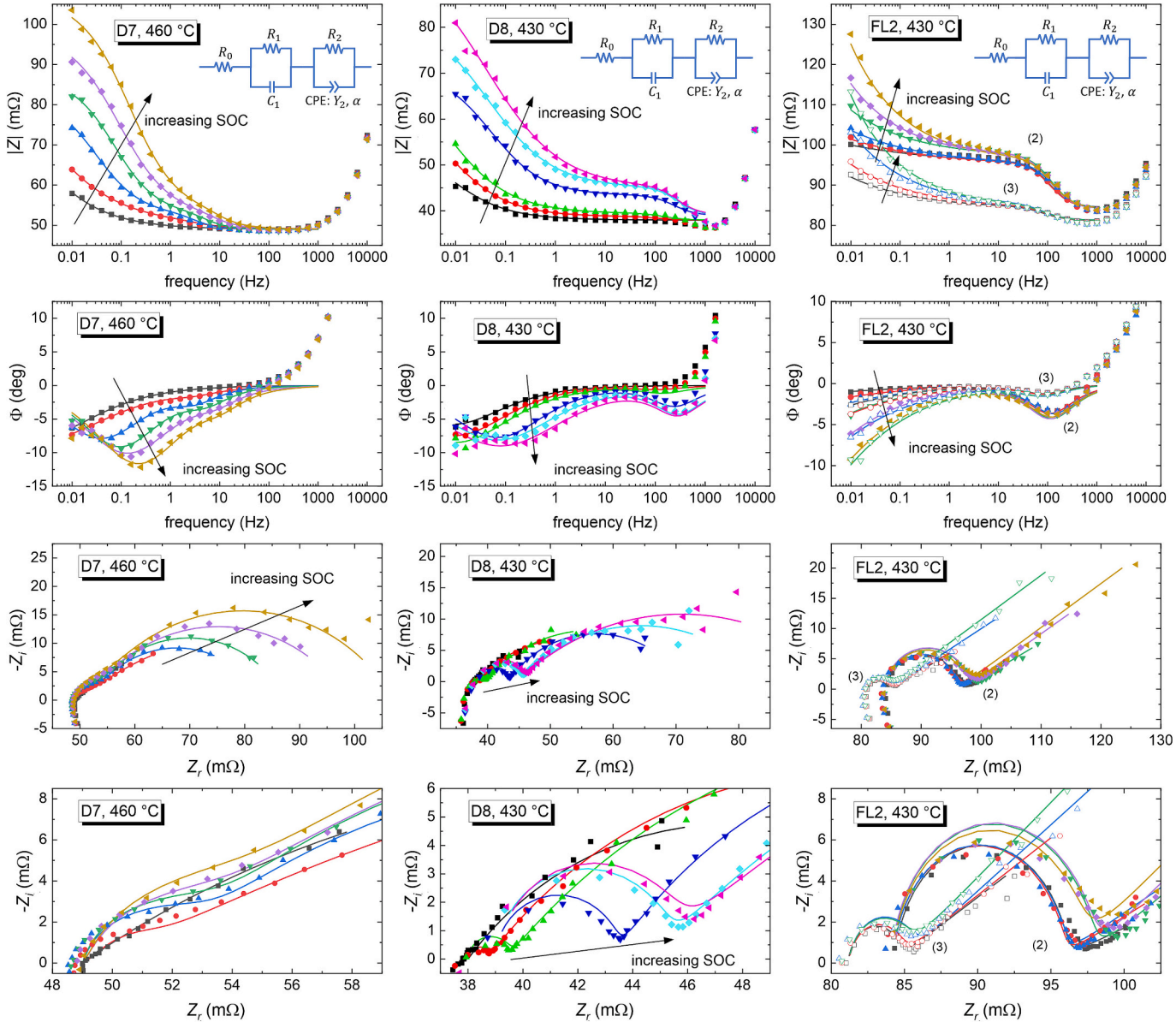

Fig. 5. EIS data (symbols) with respective fitting curves (solid lines) presented as Bode plots (1st and 2nd row) and Nyquist plot (3rd row: full scale 1:1, 4th row: zoom to high frequency region). Exemplarily shown are the data of cell D7 at 460 °C, the data of D8 at 430 °C, and the second (filled symbols) and third (open symbols) test block of FL2. Different colors correspond to different states of charge. The corresponding cell voltages are presented in Figs. 6(a) and 7.

flattened semi-circles in the capacitive regime, while the foamless cell FL2 shows an ohmic resistance, one semi-circle at medium frequencies, and a sloping line in the low frequency range. When fitting an equivalent circuit model consisting of an ohmic resistance R_0 and two generalized RC circuits to the impedance data, it turned out that an ideal RC circuit (ohmic resistance R_1 and capacitance C_1) suffices to catch the semi-circle at medium frequencies (the smaller one). The bigger semi-circle respectively sloping line at low frequencies, however, requires modelling by a generalized RC circuit with an ohmic resistance R_2 and a constant phase element with impedance $1/(Y_2(i\omega)^{\alpha})$, where the sloping lines are fitted with the resistance R_2 set to infinity. The same equivalent circuit model as shown in the figure was therefore used for fitting EIS data of all cells. The solid lines in Fig. 5 show the respective fitting curves, the fit parameters are summarized in Figs. 6 and 7.

The ohmic resistance R_0 obtained from fitting the equivalent circuit model to the EIS data does not depend on the cell's SOC (cell voltage), see Fig. 6(a). However, the data of FL2 show some dependence on cell age, see difference between test blocks (1), (2), and (3). This dependence is also depicted in Fig. 6(b), where the results from EIS of all cells are plotted together with the data obtained from IR drops at switching on currents in both cycling tests and intermittent charging/discharging tests. Very good agreement between the different methods is obtained for D7, while D8 and FL2 show slightly higher values when R_0 is determined from the IR drop.

Regarding the process at medium frequencies (~1–1000 Hz, ideal RC circuit with fit parameters R_1 and C_1), the best fits reveal a resistance R_1 around 0.7–5 mΩ and a time constant $\tau_1 = R_1C_1$ of 0.6–200 ms, see Fig. 7(a) and (b). Higher values of R_1 are obtained for cell FL2 in its early life (40 mΩ after a total operation time of 50 h, 10 mΩ after 340 h, and finally 3 mΩ after 950 h). The fitting results R_1 and τ_1 of the cell FL2 are independent of the cell's SOC (cell voltage), while the data of D7 and D8 show a small dependence on the cell voltage (R_1 increases and τ_1 decreases for increasing cell voltage). As already observed in the Bode plot, the time constant τ_1 and related cutoff frequency strongly deviate from cell to cell. The EIS data of cell D8 at 460 °C do not show the semi-circle at medium frequencies, for which reason no corresponding data appear in Fig. 7(a) and (b). The same applies to the impedance data of cell D7/460 °C and cell D8/430 °C at the lowest state-of-charge.

Finally, the fitting results revealing the process at the lowest frequencies tested by EIS (below ~1 Hz, big semi-circle respectively sloping line, generalized RC circuit with fitting parameters R_2, Y_2, and α) are presented in Fig. 7(c)–(f). For the cells with foam, D7 and D8, the resistance R_2 is in the range 20–70 mΩ, the time constant $\tau_2 = (R_2Y_2)^{1/\alpha}$ is in the range 1–200 s, and α is in the range 0.5–0.8. The resistance R_2 generally increases for increasing cell voltage, while the time constant τ_2 decreases. The exponent α is slightly different for each cell, but does not show any obvious dependence on the SOC. The foamless cell FL2 shows a slightly deviating impedance behavior in the low frequency range with infinite resistance R_2 (sloping line instead of a semi-circle). The parameter Y_2 obtained for FL2, however, is in good agreement with the respective results for D7 and D8, while the exponent α is smaller (0.2–0.4 for FL2 and 0.5–0.8 for D7/D8) and shows a small dependence on the cell voltage.

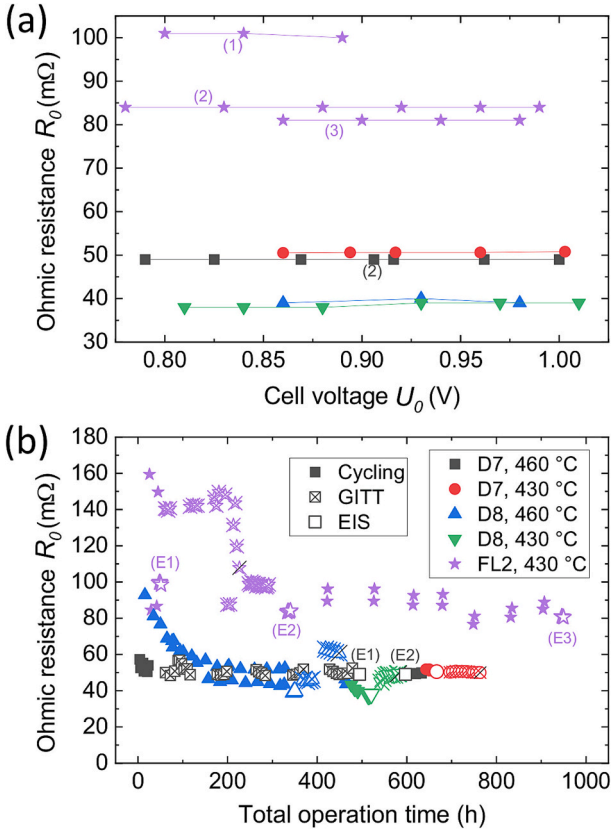

Fig. 6. Analysis of EIS data: (a) Ohmic resistance determined from EIS data, (b) comparison of ohmic resistance obtained from EIS and from IR drops of cycling and GITT measurements. The numbers (1), (2), and (3) indicate the first, second, and third block of EIS tests, see also Fig. 1(d).

4. Discussion

Na-based liquid metal batteries have been characterized on different timescales by using intermittent charging/discharging tests and electrochemical impedance spectroscopy. The results of the different tests are discussed in the following in the order of their relevant timescale.

4.1. Ohmic resistance

The cells D8 and FL2 show a higher ohmic resistance in their early life. This was found in cycling tests (Fig. 2(c)) and confirmed for FL2 by intermittent charging/discharging tests and impedance measurements (Fig. 6). The initially higher ohmic resistance might be related with exchange reactions between Na metal and foreign ions in the salt (Li^+ and K^+) or with impurities (mainly oxygen and humidity). Exchange reactions result in a partial replacement of Na by Li and K (in particular the amount of Li in the negative electrode can reach 7–17 mol%), which subsequently participate in the charge/discharge process. This might indeed increase the specific conductivity of the electrolyte and, thus, lower the ohmic resistance. Due to the much higher amount of negative electrode in FL2 compared with the cells D7 and D8, reaching equilibrium takes more time. This could explain the prolonged cell initialization process observed for FL2.

The other explanation for the initially higher ohmic resistance is impurities, in particular oxygen and humidity. Oxygen impurities are introduced in the system as dissolved oxygen or as surface oxides. The latter can increase contact resistances and, thus, the ohmic resistance of the cell. In the course of time, oxygen is caught by the strongest oxide formers in the system (Na and, due to exchange reaction, Li). Humidity is a common impurity of molten salts. Despite the applied drying procedure of the salts prior to melting, remnant humidity might have been introduced in the cells via the molten salt electrolyte. Similar to oxygen, the salt impurities caused by humidity are expected to react with the other components in the system, which results in a change of the electrolyte's properties. Cell D7, which shows the smallest effect of enhanced ohmic resistance at early times, was prepared with least oxygen in the system, see 2.2 Cell design and assembly. This hints that oxygen impurities are the main cause of the initially higher cell resistance.

After subsiding of side reactions and reaching a steady-state performance, an asymmetry between charging and discharging of the R_0 values obtained from charge/discharge cycling persists (Fig. 2(c)). This

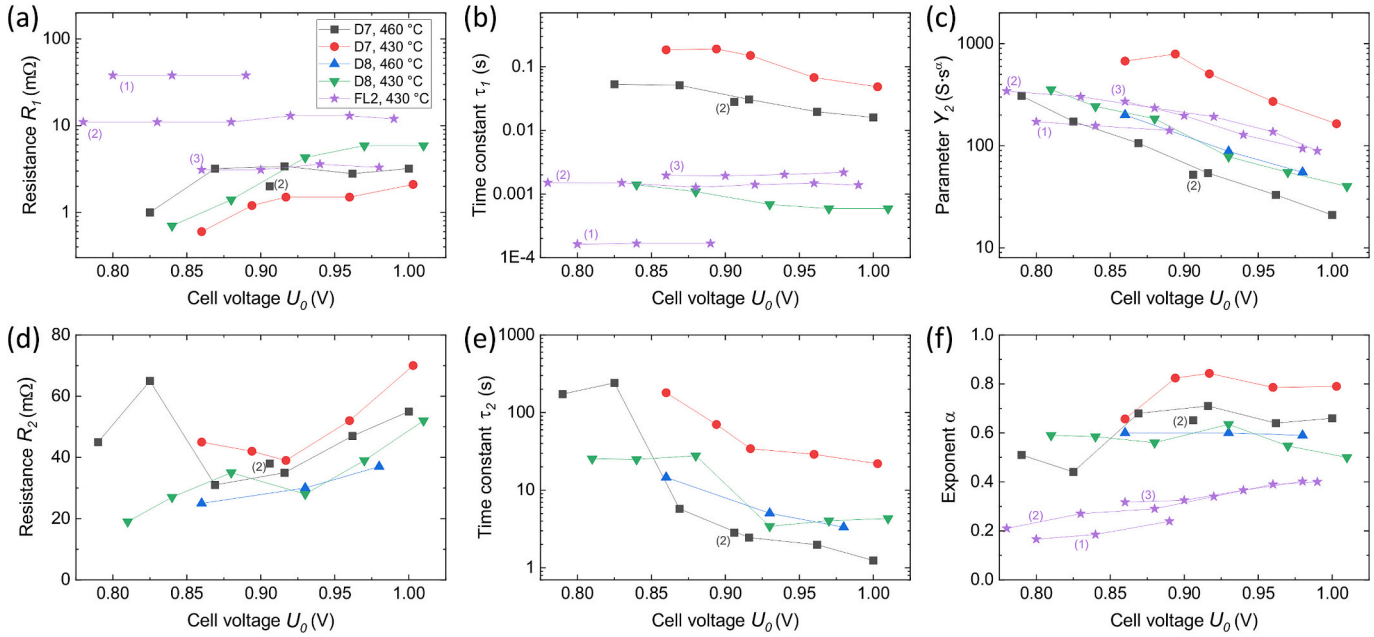

Fig. 7. Results of EIS data analysis: Parameters R_1 (a), $\tau_1 = R_1C_1$ (b), Y_2 (c), R_2 (d), $\tau_2 = R_2C_2$ (e), and α (f) obtained by fitting the equivalent circuit model to EIS data. The legend given in (a) applies to all graphs.

could be related with the fact that the cells do not reach a relaxed state in the short rest steps of the performed cycling tests. This hypothesis is supported by the symmetry of the IR drops in GITT measurements with sufficiently long relaxation steps (Fig. 3(d)).

4.2. Sub-second timescale: activation overpotential

At the shortest timescale after the ohmic reaction of the cell, the impedance data obtained by EIS are well described by an ideal RC circuit (R_1, C_1) with cutoff frequency between 1 and 300 Hz. This indicates an activation-type overpotential, i.e., the formation of a double layer with capacitance $C_{dl} = C_1$ and a charge-transfer reaction with resistance $R_{ct} = R_1$ at one or both electrode-electrolyte interfaces. Since the parameters R_1 and C_1 (or τ_1) are in the same range for both the cells with foam and the foamless cell (Fig. 7(a) and (b)), it is concluded that the identified activation overpotential is dominated by processes at the positive electrode, although a contribution from the negative electrode cannot be excluded. The charge-transfer resistance R_1 is in the range 0.7–5 mΩ for cells with foam, while the foamless cell tends to show slightly higher values (3–10 mΩ for comparable cell age). This difference can be explained reasonably by the smaller surface area S_{SbBi9} of the foamless cell. The area-normalized charge-transfer resistance is 20–140 mΩ·cm^2 for D7/D8 and 50–180 mΩ·cm^2 for FL2.

These values are much smaller than typical charge-transfer resistances of batteries with solid electrodes (several Ohm to several hundred Ohm). Furthermore, they compare well with data of other liquid metal batteries. For Li//Sb LMB cells with 6 cm inner diameter, a charge transfer resistance of 3–8 mΩ (corresponding to 85–230 mΩ·cm^2) was reported [7], while values of 22 to 37 mΩ were found for Li//Sb-Sn LMB cells [8]. Li//Sn and Li//Sn-Bi LMBs with inner diameter 2 cm showed a charge transfer resistance of 70–80 mΩ [38,39]. For a liquid displacement battery with diameter 2 cm (anode) and smaller (cathode), charge transfer resistances in the range 53–85 mΩ were obtained for both anode and cathode contributions [40].

Due to the short timescale (τ_1 below 10 ms for D8 and FL2), the activation overpotential cannot be resolved by charge/discharge cycling or GITT measurements. It is hidden in the IR drop observed after switching on the current. This explains the slightly higher ohmic resistance of D8 and FL2 when determined from IR drops compared with the values obtained from impedance data, cf. Fig. 6(b). In contrast, cell D7 shows good agreement of the R_0 values determined from the different methods, which is attributed to the larger time constant τ_1 up to 200 ms and the lower value of R_1.

An interesting observation is that the charge-transfer resistance of FL2 strongly depends on the cell age (Fig. 7(a)): Very early in its life, the cell FL2 shows a significantly higher charge-transfer resistance of 40 mΩ (720 mΩ·cm^2). It is assumed that the same side reactions (exchange reaction between Na and Li$^+$, oxygen impurities) that might explain the initially higher ohmic resistance (Fig. 6) also cause the higher charge-transfer resistance at the interface between electrolyte and positive electrode.

4.3. Intermediate timescale (~1 to ~100 s): diffusive mass transport

In contrast to the activation overpotential that builds up on the shortest timescales investigated by EIS, intermittent charging/discharging reveals the typical behavior of diffusive mass transport in the early stage of overpotential buildup, i.e., $dU_t \propto d\sqrt{t}$ for times up to ~200 s (Fig. 3(e) and (f)). This behavior is attributed to the diffusive transport of Na atoms in the positive electrode alloy Na-Sb-Bi. Diffusion coefficients D determined from the slope of the voltage data plotted versus $\sqrt{t}$ have $\log(D/\mathrm{cm^2 s^{-1}})$ values between −6.0 and −4.5, see Fig. 4(a). Different values are found for different cells, which could be caused by slightly different levels of impurities in the cells. The diffusion coefficient of each cell is found to be independent of the direction of current (charging – discharging), which is reasonable and confirms the interpretation as diffusion-dominated mass transport of Na in the positive electrode.

A diffusive process on a timescale of around 1 to 100 s is also revealed by the impedance data, which show a flattened semi-circle (respectively sloping line for FL2) in the low frequency range of the Nyquist plot, Fig. 5. The constant phase element used to model either the semi-circle or the sloping line has an exponent α close to 0.5 (Fig. 7(f)), which suggests diffusive contributions in both cases.

Literature reports diffusion coefficients of Li in the positive electrode of Li//Sb-Sn LMB cells with $\log(D/\mathrm{cm^2 s^{-1}})$ in the range −4.8 to −3.4 [27]. Slightly lower diffusion coefficients are reported for Li//Sb-Sn-Ti LMB cells, with $\log(D/\mathrm{cm^2 s^{-1}})$ in the range −6 to −4 [28]. The only

study that reports diffusion coefficients of Na in Na-based LMBs (Na//Bi and Na//Sb-Bi cells) finds similar values at high SOC [12]. Analysis was done for discharge only, with estimated values of $\log(D/\mathrm{cm^2 s^{-1}})$ around −5 at high SOC. The values decreased to around −9 as discharge proceeded, which was attributed to formation of a solid intermetallic layer at the surface of the positive electrode.

4.4. Timescale beyond ~100 s: convective mass transport

For times larger ~100 s, the increase proportional to $\sqrt{t}$ of the mass transport overpotential is replaced by a stage of roughly constant overpotential, see Fig. 3(e) and (f). As rationalized in the following, this transition is attributed to convection.

Fluid flow in an LMB cell can be caused by different effects such as temperature gradients due to external boundary conditions or internal heating, electromagnetic interaction, or concentration gradients. In order to assess the relevance of these effects and their influence on fluid flow and mass transport in the present LMB system, respective numerical simulations were performed using the simulation software COMSOL Multiphysics. Due to the approximations and assumptions used, the simulation results should be understood as reasonable estimates only. The assumptions included rotational symmetry, neglect of any dynamics inside the negative electrode, the external boundary conditions on heat transfer, and the material properties used. The latter are summarized in Table 2.

Regarding the external boundary conditions on heat transfer, the cell bottom was fixed at the given temperature, the cell wall was considered adiabatic, and the heat loss at the cell cover was estimated taking into account radiation and air cooling by natural convection, which summed up to a total heat loss of ~65 W. These boundary conditions were rationalized by comparison of the simulation results with the temperature data measured inside the cell, see 2.2 Cell design and assembly. With the given boundary conditions, the buoyancy-driven thermal convection due to the external boundary conditions is found to be considerable both in the electrolyte (average velocity 2.1 and 2.5 mm/s, respectively, for D7 and FL2) and in the positive electrode (average velocity 0.8 and 1.1 mm/s for D7 and FL2), see Fig. 8(a) for a snapshot of thermal convection in both fluids with flow coupling at their interface. This result is in contrast to most LMB cells reported in literature that are at isothermal boundary conditions.

For assessment of internal heating (Joule heating) and electromagnetic interactions, a charge/discharge current of 1 A was applied and the current density distribution in the cell and the induced magnetic field were determined. Any external magnetic field (e.g., terrestrial) was neglected. For the investigated cells under the given conditions, the effects of Joule heating and electro-vortex flow are found to be negligible against the thermal convection induced by the external boundary conditions. This applies to both electrolyte and positive electrode. Therefore, Joule heating and magnetohydrodynamic effects were neglected in the mass transport simulations presented in the following. Additionally, due to the large thermal convection in the electrolyte, the transport of Na^+ ions and related mass transport overpotential in the electrolyte was not considered.

The time-dependent concentration field of Na in the positive electrode was modelled as transport of diluted species. Hereby, the stationary Na flux density to/from the surface was calculated from the current density distribution in the cells D7 and FL2 discharged/charged with 0.5 and 0.7 A, respectively. Starting from an initially homogeneous Na concentration in the positive electrode, $x_{Na,0}$, the red curve denoted "diffusion only" in Fig. 8(b) shows the evolution of the average Na concentration at the surface of the positive electrode, $\langle x_{Na}(t) \rangle$, for a purely diffusive mass transport after switching on the stationary Na flux to/from this surface. The expected behavior proportional to $\sqrt{t}$, which finally leads to Eq. (1), is obtained for both charging and discharging in the time range investigated. Considering diffusive-convective mass transport of Na in the stationary velocity field of the positive electrode induced by externally driven thermal convection (here the electrolyte was assumed to be at rest and a no-slip boundary condition was applied at the interface between positive electrode and electrolyte), the blue curve denoted "diff. + thermal conv." is obtained for both charging and discharging. In the initial stage (first 20 s) after switching on the current, diffusive-convective mass transport (blue curve) shows the same evolution of the average surface concentration as the corresponding purely diffusive transport (red curve). In a later stage, however, convective transport becomes relevant and results in a roughly constant offset between the average concentration at the surface and the average bulk concentration (black curve "bulk average"), which translates into a roughly constant mass transport overpotential.

Finally, the effect of solutal convection was evaluated by introducing a concentration-dependent density of the positive electrode. With a homogenous Na concentration and the stationary flow field of thermal convection used as initial conditions, the time-dependent fully-coupled equations of diffusive-convective mass transport of Na and buoyancy-driven fluid flow with temperature- and concentration-dependent density were solved for the positive electrode. Also here, the electrolyte was set at rest. The inhomogeneous concentration of Na in the positive

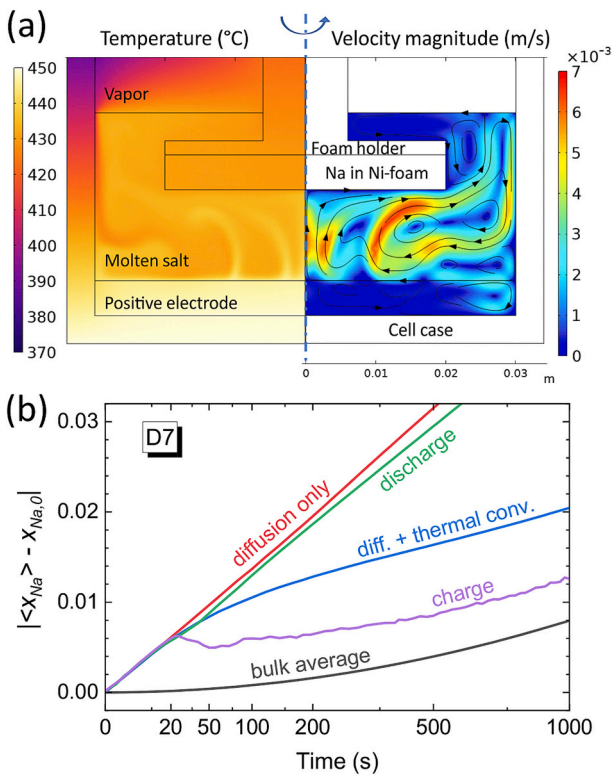

Fig. 8. Simulation results for cell D7. (a) Snapshot of time-dependent conjugate heat transfer and buoyancy-driven non-isothermal flow when no electric current runs through the LMB cell. (b) Mass transport in the positive electrode charged/discharged with 0.5 A. Shown is the difference between the surface (bulk) average of x_{Na} and its initial value $x_{Na,0}$ as function of time (square-root scale).

Table 2
Estimated material properties at 450 °C used for simulations.

	Electrolyte	Positive electrode
viscosity η (Pa•s)	0.003	0.003
reference density ρ_{ref} (kg/m^3)	1650	9200
thermal expansion coefficient α (1/K)	3.2e−4	1.4e−4
solutal expansion coefficient β (m^3/mol)	–	2.2e−5
Na diffusion coefficient D (cm^2/s)	–	1e−5

electrode upon charging/discharging with 0.5 to 0.7 A (as used in GITT experiments) is found to significantly influence convection and mass transport, see the violet and green curves in Fig. 8(b) denoted "charge" and "discharge". A deviation from the purely thermal convection starts to build up after ~30 s and leads to an asymmetry between charging and discharging in the long-term behavior. Charging enhances convection considerably, leading to an increased mass transport and a reduced concentration offset, while discharging stabilizes the density distribution and mitigates convection. For the given parameters and with the applied assumptions, thermal convection is entirely damped by the compositional effect on density upon discharging, and the average concentration of Na at the surface follows roughly the purely diffusive case. This contradicts the experimental data on discharge (Fig. 3), which clearly show a transition from a diffusive regime ($\eta_{mt} \propto \sqrt{t}$) to a regime of convection-enhanced mass transport ($\eta_{mt} \approx$ const.). However, in case of a stable density stratification during discharge with high enough currents, effects neglected in the present simulations may become relevant. These could be interfacial phenomena such as Marangoni flow due to the dependence of the interfacial tension on temperature and/or composition or, in particular, flow coupling between electrolyte and positive electrode. Preliminary simulations including thermal convection in the electrolyte and flow coupling indeed indicate that the convection in the electrolyte is strong enough to drive considerable flow in the positive electrode despite the stabilizing solutal effect upon discharge, which finally, after about 200 s, leads to a roughly constant concentration offset between surface average and bulk average.

The predicted asymmetry due to the influence of solutal expansion agrees very well with the experimental data, which show higher long-term overpotentials η_{cmt} for discharging than for charging, see corresponding resistance R_{cmt} in Fig. 4(c). The generally lower values of R_{cmt} obtained for the foamless cell FL2 compared with D7/D8 could be related with the slightly higher level of thermal convection in FL2, see average velocities given above. Finally, the dependence of R_{cmt} on the cell's SOC could be linked with the nonlinear relation between the cell voltage U_0 and the Na concentration x_{Na}, see Fig. 3(c). At higher cell voltage, the same concentration offset between surface average and bulk average leads to a higher voltage difference, i.e., a higher mass transport overpotential η_{cmt} and related resistance.

For the impedance measurements, an AC current of 20 mA RMS amplitude was used. With such a low current, respective simulations show no difference between charging and discharging for at least 1000 s. Since the lowest frequency probed by EIS was 0.01 Hz, no influence of solutal convection on the impedance data is expected. However, thermal convection can well influence the impedance in the low frequency range. Indeed, the impedance data of D7 and D8 show in the low frequency limit the trend to converge to a finite resistance. The respective values R_2 obtained from fitting the impedance data (Fig. 7(d)) are in rather good agreement with the long-term overpotential η_{cmt} and its resistance R_{cmt} found in GITT data, see Fig. 4(c). The agreement concerns not only the magnitude but also the dependence on the cell voltage and the cell-specific differences. Additionally, the time constant τ_2 determined from the EIS data of D7 and D8, Fig. 7(e), is in reasonable agreement with the transition times between diffusive and convective mass transport observed in GITT, see Fig. 4(b). Also here, both the dependence on the cell voltage and the differences between the different cells/temperatures are reproduced very well. Together with the capability of a constant phase element to model diffusive mass transport, the consistencies of the steady-state resistance and transition time confirm that a generalized RC circuit is a good equivalent circuit model to describe the impedance attributable to mass transport in two different regimes, diffusion-dominated at short timescale (below the time constant of the generalized RC circuit) and convection-enhanced in the longer term (above the respective time constant). However, it remains an open question why the impedance data of the foamless cell FL2 do not show convergence to a finite resistance in the probed frequency range.

5. Conclusion

The scope of this investigation was the experimental characterization of the electrochemical processes in a liquid metal battery that occur on different timescales. As a model system, Na-based liquid metal batteries with an $SbBi_9$ alloy as positive electrode were assembled. Two different designs were realized, one utilizing a metal foam to host the negative electrode (liquid sodium) and the other without foam but insulating sheath. All cells were tested by charge-discharge cycling, the galvanostatic intermittent titration technique (GITT), and electrochemical impedance spectroscopy (EIS). The two electrochemical characterization techniques GITT and EIS complement each other in terms of the probed timescale, which allowed to identify and quantify processes occurring on the millisecond range up to the ones that dominate after 1000 s.

Omitting inductive processes, the fastest process captured by EIS after the immediate cell reaction due to its ohmic resistance is the formation of a double layer at the electrode-electrolyte interface, i.e., the buildup of the activation overpotential at that interface, with time constants between 0.6 and 200 ms. The corresponding charge transfer resistance is in the range 0.7–5 mΩ, increasing for an increasing state-of-charge (SOC) of the cell. The next overpotential, captured by both EIS and GITT, builds up on the timescale of 1–200 s and is attributed to diffusive transport of Na in the positive electrode. The diffusion coefficient does neither depend on the direction of current nor on the cell's SOC within the investigated range. For timescales beyond ~100 s, the diffusive mass transport transitions to a convection-enhanced mass transport with roughly constant overpotential. The overpotential asymmetry found between charging and discharging in GITT tests clearly indicates an influence of solutal convection when charging/discharging currents of 0.5 to 0.7 A are applied. However, the main source of convection is attributed to the strong temperature gradient induced by the external boundary conditions. Impedance measurements of the cells with foam tend to converge to a finite resistance in the low frequency limit, which agrees with the conclusion that significant thermal convection is present independent of the electrochemical activity of the cell. Heating LMB cells from below to induce considerable thermal convection in the positive electrode is not feasible in large-scale applications, where many cells are combined to stacks with a global temperature management.

CRediT authorship contribution statement

Renate Fetzer: Writing – original draft, Methodology, Investigation, Conceptualization. **Alfons Weisenburger:** Writing – review & editing, Resources. **Georg Müller:** Writing – review & editing, Funding acquisition.

Declaration of competing interest

The authors declare that they have no known competing financial interests or personal relationships that could have appeared to influence the work reported in this paper.

Acknowledgements

The authors express their gratitude to Tianru Zhang and Florian Lindner for their contributions to design and assembly of the LMB cells. The authors are grateful to the Deutsche Forschungsgemeinschaft (DFG) and National Natural Science Foundation of China (NSFC) for funding the DFG-NSFC Sino-German Project (DFG Project Member 411450529): "Study on Corrosion Control and Low-Temperature Electrolytes for Low-Cost Na-based Liquid Metal Batteries".

Data availability

Data will be made available on request.

References

[1] H. Kim, D.A. Boysen, J.M. Newhouse, B.L. Spatocco, B. Chung, P.J. Burke, D. J. Bradwell, K. Jiang, A.A. Tomaszowska, K. Wang, W. Wei, L.A. Ortiz, S.A. Barriga, S.M. Poizeau, D.R. Sadoway, Liquid metal batteries: past, present, and future, Chem. Rev. 113 (2013) 2075–2099, https://doi.org/10.1021/cr300205k.

[2] H. Li, H. Yin, K. Wang, S. Cheng, K. Jiang, D.R. Sadoway, Liquid metal electrodes for energy storage batteries, Adv. Energy Mater. 6 (2016), https://doi.org/10.1002/aenm.201600483.

[3] Y. Ding, X. Guo, G. Yu, Next-generation liquid metal batteries based on the chemistry of fusible alloys, ACS Cent. Sci. 6 (2020) 1355–1366, https://doi.org/10.1021/acscentsci.0c00749.

[4] Q. Zeng, Z. Lv, S. Li, B. Yang, J. He, J. Song, Electrolytes for liquid metal batteries, Mater. Res. Bull. 170 (2024) 112586, https://doi.org/10.1016/j.materresbull.2023.112586.

[5] K. Wang, K. Jiang, B. Chung, T. Ouchi, P.J. Burke, D.A. Boysen, D.J. Bradwell, H. Kim, U. Muecke, D.R. Sadoway, Lithium-antimony-lead liquid metal battery for grid-level energy storage, Nature 514 (2014) 348–350, https://doi.org/10.1038/nature13700.

[6] T. Dai, Y. Zhao, X.H. Ning, R. Lakshmi Narayan, J. Li, Z. wei Shan, Capacity extended bismuth-antimony cathode for high-performance liquid metal battery, J. Power Sources 381 (2018) 38–45, https://doi.org/10.1016/j.jpowsour.2018.01.048.

[7] S. Yan, X. Zhou, H. Li, Y. Shen, Y. He, H. Zhou, K. Wang, K. Jiang, Utilizing in situ alloying reaction to achieve the self-healing, high energy density and cost-effective Li||Sb liquid metal battery, J. Power Sources 514 (2021) 230578, https://doi.org/10.1016/j.jpowsour.2021.230578.

[8] H. Li, K. Wang, S. Cheng, K. Jiang, High performance liquid metal battery with environmentally friendly antimony-tin positive electrode, ACS Appl. Mater. Interfaces 8 (2016) 12830–12835, https://doi.org/10.1021/acsami.6b02576.

[9] W. Zhao, P. Li, Z. Liu, D. He, K. Han, H. Zhao, X. Qu, High-performance antimony–bismuth–tin positive electrode for liquid metal battery, Chem. Mater. 30 (2018) 8739–8746, https://doi.org/10.1021/acs.chemmater.8b01869.

[10] K. Cui, W. Zhao, S. Li, D. Zhou, C. Liu, X. Qu, P. Li, Low-temperature and high-energy-density Li-based liquid metal batteries based on LiCl–KCl molten salt electrolyte, ACS Sustain. Chem. Eng. 10 (2022) 1871–1879, https://doi.org/10.1021/acssuschemeng.1c07560.

[11] K. Cui, P. Li, W. Zhao, S. Li, C. Liu, X. Qu, Electrochemical performance and application prospect analysis of Li||Sb-Bi-Sn liquid metal batteries, Mater. Lett. 338 (2023) 134067, https://doi.org/10.1016/j.matlet.2023.134067.

[12] H. Zhou, H. Li, Q. Gong, S. Yan, X. Zhou, S. Liang, W. Ding, Y. He, K. Jiang, K. Wang, A sodium liquid metal battery based on the multi-cationic electrolyte for grid energy storage, Energy Storage Mater. 50 (2022) 572–579, https://doi.org/10.1016/j.ensm.2022.05.032.

[13] R. Fetzer, T. Zhang, F. Lindner, A. Weisenburger, G. Müller, How cell design affects the performance of sodium-antimony-bismuth liquid metal batteries, J. Power Sources 591 (2024) 233823, https://doi.org/10.1016/j.jpowsour.2023.233823.

[14] D.H. Kelley, T. Weier, Fluid mechanics of liquid metal batteries, Appl. Mech. Rev. 70 (2018), https://doi.org/10.1115/1.4038699.

[15] Y. Shen, O. Zikanov, Thermal convection in a liquid metal battery, Theor. Comput. Fluid Dyn. 30 (2016) 275–294, https://doi.org/10.1007/s00162-015-0378-1.

[16] X. Zhou, C. Gao, K. Wang, K. Jiang, H. Li, A comparative study of thermally and electromagnetically driven flow in the electrolyte of liquid metal batteries and their effects on ion transport, IEEE Trans. Ind. Appl. 60 (2024) 1760–1769, https://doi.org/10.1109/TIA.2023.3319299.

[17] D.H. Kelley, D.R. Sadoway, Mixing in a liquid metal electrode, Phys. Fluids 26 (2014) 057102, https://doi.org/10.1063/1.4875815.

[18] N. Weber, M. Nimtz, P. Personnettaz, A. Salas, T. Weier, Electromagnetically driven convection suitable for mass transfer enhancement in liquid metal batteries, Appl. Therm. Eng. 143 (2018) 293–301, https://doi.org/10.1016/j.applthermaleng.2018.07.067.

[19] W. Herreman, C. Nore, L. Cappanera, J.-L. Guermond, Efficient mixing by swirling electrovortex flows in liquid metal batteries, J. Fluid Mech. 915 (2021) A17, https://doi.org/10.1017/jfm.2021.79.

[20] X. Zhou, L. Fan, S. Yan, W. Zhang, B. Li, H. Li, K. Wang, K. Jiang, Enhancing capacity utilization of Li|LiCl-KCl-CsCl|Bi (300 °C) liquid metal batteries through the application of external magnetic fields, J. Power Sources 624 (2024) 235516, https://doi.org/10.1016/j.jpowsour.2024.235516.

[21] P. Personnettaz, S. Landgraf, M. Nimtz, N. Weber, T. Weier, Mass transport induced asymmetry in charge/discharge behavior of liquid metal batteries, Electrochem. Commun. 105 (2019), https://doi.org/10.1016/j.elecom.2019.106496.

[22] X. Zhou, C. Gao, Y. Shen, H. Li, S. Yan, H. Zhou, K. Wang, K. Jiang, Multi-field coupled model for liquid metal battery: comparative analysis of various flow mechanisms and their effects on mass transfer and electrochemical performance, Energy Rep. 8 (2022) 5510–5521, https://doi.org/10.1016/j.egyr.2022.04.018.

[23] W. Herreman, S. Bénard, C. Nore, P. Personnettaz, L. Cappanera, J.-L. Guermond, Solutal buoyancy and electrovortex flow in liquid metal batteries, Phys. Rev. Fluids 5 (2020) 74501, https://doi.org/10.1103/PhysRevFluids.5.074501.

[24] D.F. Keogh, M. Baldry, V. Timchenko, J. Reizes, C. Menictas, Modelling the effects of areal capacity on mass transport in liquid metal batteries, J. Power Sources 573 (2023) 233142, https://doi.org/10.1016/j.jpowsour.2023.233142.

[25] V. Ranawade, R. Verma, N. Tiwari, K.S. Nalwa, A comprehensive multiphysics approach to model solutal buoyancy, thermal convection, and electro-vortex flow phenomena for liquid metal batteries, J. Energy Storage 85 (2024) 111100, https://doi.org/10.1016/j.est.2024.111100.

[26] P. Personnettaz, T.S. Klopper, N. Weber, T. Weier, Layer coupling between solutal and thermal convection in liquid metal batteries, Int. J. Heat Mass Transf. 188 (2022) 122555, https://doi.org/10.1016/j.ijheatmasstransfer.2022.122555.

[27] K. Cui, F. An, W. Zhao, P. Li, S. Li, C. Liu, X. Qu, Feasibility research of SS304 serving as the positive current collector of Li||Sb-Sn liquid metal batteries, J. Phys. Chem. C 125 (2021) 237–245, https://doi.org/10.1021/acs.jpcc.0c09629.

[28] S. Yan, H. Li, Z. Li, W. Chen, X. Zhou, H. Zhou, W. Zhang, Y. He, K. Jiang, K. Wang, In situ transition layer design based on Ti additive enabling high-performance liquid metal batteries, ACS Appl. Mater. Interfaces 15 (2023) 5265–5272, https://doi.org/10.1021/acsami.2c19774.

[29] C.H. Chen, J. Liu, K. Amine, Symmetric cell approach and impedance spectroscopy of high power lithium-ion batteries, J. Power Sources 96 (2001) 321–328, https://doi.org/10.1016/S0378-7753(00)00666-2.

[30] J.C. Burns, L.J. Krause, D.-B. Le, L.D. Jensen, A.J. Smith, D. Xiong, J.R. Dahn, Introducing symmetric Li-ion cells as a tool to study cell degradation mechanisms, J. Electrochem. Soc. 158 (2011) A1417, https://doi.org/10.1149/2.084112jes.

[31] J. Conder, C. Villevieille, S. Trabesinger, P. Novák, L. Gubler, R. Bouchet, Electrochemical impedance spectroscopy of a Li–S battery: part 1. Influence of the electrode and electrolyte compositions on the impedance of symmetric cells, Electrochim. Acta 244 (2017) 61–68, https://doi.org/10.1016/j.electacta.2017.05.041.

[32] S. Drvarič Talian, J. Moškon, R. Dominko, M. Gaberšček, Reactivity and diffusivity of Li polysulfides: a fundamental study using impedance spectroscopy, ACS Appl. Mater. Interfaces 9 (2017) 29760–29770, https://doi.org/10.1021/acsami.7b08317.

[33] S. Waluś, C. Barchasz, R. Bouchet, F. Alloin, Electrochemical impedance spectroscopy study of lithium–sulfur batteries: useful technique to reveal the Li/S electrochemical mechanism, Electrochim. Acta 359 (2020) 136944, https://doi.org/10.1016/j.electacta.2020.136944.

[34] M. Heinrich, N. Wolff, S. Seitz, U. Krewer, Identifying anode and cathode contributions in Li-ion full-cell impedance spectra, Batteries 8 (2022), https://doi.org/10.3390/batteries8050040.

[35] D.J. Bradwell, H. Kim, A.H.C. Sirk, D.R. Sadoway, Magnesium–antimony liquid metal battery for stationary energy storage, J. Am. Chem. Soc. 134 (2012) 1895–1897, https://doi.org/10.1021/ja209759s.

[36] G. Müller, G. Schumacher, F. Zimmermann, Investigation on oxygen controlled liquid lead corrosion of surface treated steels, J. Nucl. Mater. 278 (2000) 85–95, https://doi.org/10.1016/S0022-3115(99)00211-1.

[37] C.J. Wen, B.A. Boukamp, R.A. Huggins, W. Weppner, Thermodynamic and mass transport properties of "LiAl", J. Electrochem. Soc. 126 (1979) 2258, https://doi.org/10.1149/1.2128939.

[38] J.-S. Yeo, J.-H. Lee, E.-J. Yoo, Electrochemical properties of environment-friendly lithium-tin liquid metal battery, Electrochim. Acta 290 (2018) 228–235, https://doi.org/10.1016/j.electacta.2018.09.072.

[39] J.-S. Yeo, E. Yoo, C.N. Im, J.-H. Cho, Enhanced electrochemical properties of lithium-tin liquid metal battery via the introduction of bismuth cathode material, Electrochim. Acta 389 (2021) 138697, https://doi.org/10.1016/j.electacta.2021.138697.

[40] K. Mushtaq, J. Zhao, N. Weber, A. Mendes, D.R. Sadoway, Self-discharge mitigation in a liquid metal displacement battery, J. Energy Chem. 66 (2022) 390–396, https://doi.org/10.1016/j.jechem.2021.08.015.